A Fiber Optic Spectrometry System for Measuring Irradiance Distributions in Sea Ice Environments

HANGZHOU WANG

State Key Laboratory of Fluid Power Transmission and Control, Zhejiang University, Hangzhou, Zhejiang, China

YING CHEN

State Key Laboratory of Fluid Power Transmission and Control, and Ocean College, Zhejiang University, Hangzhou, Zhejiang, China

HONG SONG

Ocean College, Zhejiang University, Hangzhou, Zhejiang, China

SAMUEL R. LANEY

Biology Department, Woods Hole Oceanographic Institution, Woods Hole, Massachusetts

ABSTRACT

A fiber optic–based spectrometry system was developed to enable automated, long-term measurements of spectral irradiance in sea ice environments. This system utilizes a single spectrometer module that measures the irradiance transmitted by multiple optical fibers, each coupled to the input fiber of the module via a mechanical rotary multiplexer. Small custom-printed optical diffusers, fixed to the input end of each fiber, allow these probes to be frozen into ice auger holes as small as 5 cm in diameter. Temperature-dependent biases in the spectrometer module and associated electronics were examined down to −40°C using an environmental chamber to identify any artifacts that might arise when operating these electronic and optical components below their vendor-defined lower temperature limits. The optical performance of the entire system was assessed by freezing multiple fiber probes in a 1.2-m-tall ice column, illuminating from above with a light source, and measuring spectral irradiance distributions at different depths within the ice column. Results indicated that the radiometric sensitivity of this fiber-based system is comparable to that of commercially available oceanographic spectroradiometers.

1. Introduction

Photosynthetic algae are a key component of sea ice ecosystems. Rich algal communities can be found in melt ponds that form on the ice or snow surface, in complex brine networks internal to the porous ice itself, in layers attached to the bottom of sea ice, and in the water column immediately below (Arrigo and Thomas 2004). The biomass, taxonomic composition, and photosynthetic behavior of these algal communities are each shaped by complex interactions between incident solar insolation, snow accumulation, brine dynamics, and physical processes driving ice formation and decay, through the effects each has on the availability of light and nutrients (Fritsen et al. 1994; Haas et al. 2001; Maksym and Jeffries 2001; Saenz and Arrigo 2012). Direct measurement of the full seasonal trajectory of ice algal communities and their physical environment is challenging, however, because of methodological limitations with how we observe ice algae and their habitats. Ice cores have arguably provided the greatest direct insight into ice algal ecology, but cores are sampled typically over periods of weeks at most (e.g., Fritsen et al. 2011; Palmisano et al. 1987) and rarely over multiple months. As a result, our understanding of the

Corresponding author address: Samuel Laney, Biology Department, Woods Hole Oceanographic Institution, MS 34, Redfield 1-38, Woods Hole, MA 02543.
E-mail: slaney@whoi.edu

seasonal and annual dynamics that occur in ice algal communities remains poorly developed.

A critical environmental parameter to measure in ice algal ecology is the intensity and spectral composition of the ambient light field within the ice layer itself. Sunlight at wavelengths between 400 and 700 nm [typically referred to as photosynthetically active radiation (PAR), in the photosynthetic literature] provides the energy that ice algae use to support photosynthesis and growth. The absolute intensity of light is a first-order control on algal growth, but algae absorb and utilize only certain wavelengths of PAR. As a result, algae that occur higher in sea ice can in effect shade the algae living beneath them in the ice or in the water column below. This phenomenon has an ecological effect on the vertical structure of algal communities in a given ice layer, and it also provides a means to estimate algal biomass in sea ice via optical models that include ice algae in spectral models for light attenuation through sea ice (Ehn et al. 2008; Legendre et al. 1992; Mundy et al. 2007; Perovich et al. 1993).

Much of the motivation to measure light fields above and under sea ice comes from an interest in sea ice albedo and radiative energy fluxes (e.g., Frey et al. 2011; Grenfell and Perovich 1984; Maykut and Grenfell 1975; Perovich et al. 2002). The bio-optical aspects of sea ice have also received attention albeit to a lesser degree (e.g., Fritsen et al. 2011; Palmisano et al. 1987; Perovich et al. 1993). Most of the light measurements described in field studies were made using approaches that are primarily manual, but more recently the use of robotic vehicles (Nicolaus and Katlein 2013; Nicolaus et al. 2012) and unattended dataloggers (Nicolaus et al. 2010a,b) have been explored. Relatively few studies have examined the distribution of light within the ice layer itself (Legendre et al. 1992; Light et al. 2008; Perovich et al. 1998) and, moreover, in these studies the sampling duration and frequencies of measurements have been limited by the manual approach employed and thus by safety and accessibility factors associated with human involvement in collecting these data.

Autonomous systems hold considerable promise for expanding our ability to make long-term observations of spectral irradiance in ice algal habitats, over the seasonal and annual scales that currently remain underexamined. Motivated by the success of autonomous systems for measuring ice mass balance properties (Jackson et al. 2013; Richter-Menge et al. 2006), we began developing an analogous approach for measuring spectral irradiance in sea ice habitats, autonomously and over similar seasonal-to-annual scales. We here describe a spectrometry system that utilizes a fiber optic approach to measure spectral irradiance in sea ice environments concurrently at multiple depths in the ice, relatively noninvasively and potentially over full seasonal scales.

2. System design

a. Objectives and requirements

Our primary objective was to enable autonomous, long-term measurement of spectral irradiance not only at multiple depths within a layer of sea ice but also above and below the ice layer. These latter measurements would complement the in-ice data by providing reference measurements of incoming insolation as well as direct measurements of the irradiance that passes through the ice layer and into the water column below. Spectrally, measurements in the visible wavelengths (400–700 nm) would provide the necessary data for inferring the presence and abundance of algal layers within and below the ice layer from their spectral absorption by pigments. If these measurements could be extended into the ultraviolet, it would also be possible to use this same system to study the potential influence of ultraviolet exposure on algal community biomass, which is an important area of study in polar algal ecology (e.g., Karentz et al. 1991). These requirements suggested use of a grating spectrometer instead of the large number of discrete, narrowband photodiodes that would otherwise be needed to obtain the requisite spectral resolution over this range of wavelengths. Several monolithic spectrometer modules are available commercially, but an important concern is that the temperature biases of commercial modules have typically not been determined for the range of low environmental temperatures for which this system is intended. Such modules can be quite small ($\sim$10 cm^3) but placing them directly in the ice was not deemed feasible given the vertical sampling resolution we desired ($\sim$10–20 cm) and the potential shading that would arise when placing such modules in proximity to one another.

Given these considerations and the importance of disturbing the ice as little as possible, a preferred approach was a system that could be deployed into standard 2-in. ($\sim$5 cm) auger holes. This requirement suggested the use of multiple fibers, embedded in the ice at different depths but all connecting to a single spectrometer module located on the ice surface above (Fig. 1). Additional fibers placed above the ice can measure reflected radiance or incident irradiance, and fibers with ends below the ice can measure irradiance in the water column below. Additional sensors, such as thermistor strings, sonar altimeters, snow depth sensors, and position/location receivers, would provide important ancillary data regarding changes in the physical properties of the snow/ice layer that affect ice algal communities.

b. Spectroscopic and optical considerations

The spectrometry system uses a compact miniature spectrometer module (C11009MA, Hamamatsu Photonics K.K.) containing an S8378-256N complementary
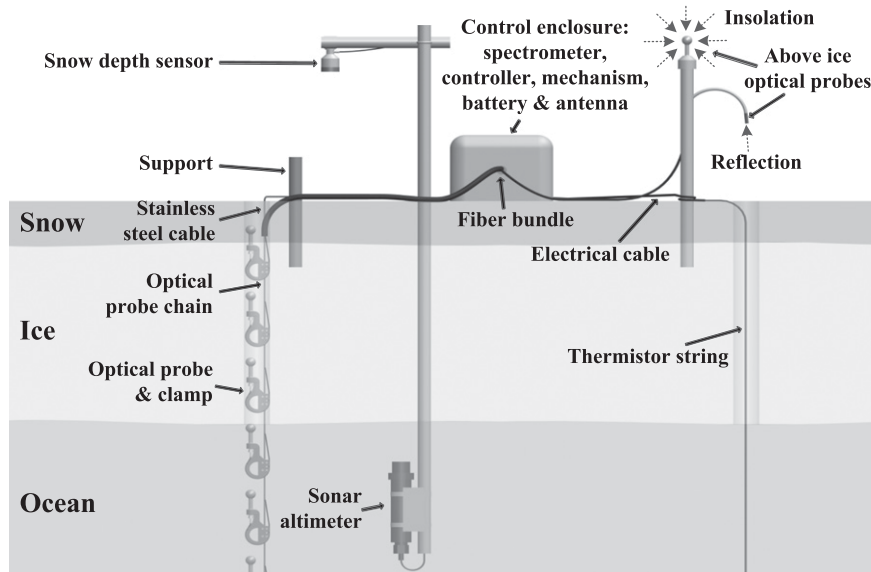
FIG. 1. A potential deployment scenario where an enclosure containing the core spectrometer and associated electronics, mechanics, battery pack, satellite modem, and GPS connects to a 12-fiber bundle. Ten of the fibers are lowered through a 5-cm auger hole drilled through snow and sea ice, placed at depths to sample both the internal light field in the ice and the water column below. Two fibers observe the incident and reflected spectral irradiance above the surface. Snow depth and ice thickness are measured using ancillary sensors in conjunction with a thermistor string placed in a second auger hole nearby. Strategies to minimize measurement artifacts in longer-term deployments (e.g., due to biofouling of below-ice fibers or riming of above-ice fibers) are omitted for simplicity.

metal–oxide–semiconductor (CMOS) image sensor. This particular spectrometer provides a maximum spectral resolution of 9 nm within a wavelength range spanning 340–780 nm, representing 256 pixels (Table 1). The module generates an analog voltage output for each pixel, where the voltage output is a function of the incident light intensity, the measurement's integration time, and the gain setting of the module ("high" or "low" gain). For an application where signals are expected to cover a high dynamic range, such as in the intended situation of measuring vertical distributions of light within sea ice, this additional gain setting is advantageous. An onboard 12-bit temperature sensor in the spectrometer module (DS1775R, Maxim Integrated Products) provides important real-time data regarding the module's temperature.

In this prototype system, up to 12 individual fiber probes can be sampled by means of a rotary mechanical multiplexer that consists of a geared servomotor, a gear pair, and an optical encoder (Fig. 2a). A fiber collimating lens assembly (74-ACR, Ocean Optics, Inc.) was used in front of the spectrometer module's 600-μm fiber input to maximize the coupling between these probe fibers and the module. The servomotor (RE-max 24 with GP22C gearhead; Maxon Motor AG) rotates a wheel

that holds the output ends of all the fiber probes, aligning the output of a selected fiber with the input fiber of the spectrometer module. The motor provides up to 2.0 N m of torque that is further amplified (~2 times) by a gear pair attached to the drive shafts. This design is powerful enough to overcome the torque generated by twisted fibers and by any friction in the shafts and bearings, even at temperatures down to −40°C. The encoder (HEDS-5540-G06, Avago Technologies) is mounted

TABLE 1. Performance and operational characteristics of the C11009MA spectrometer module used in this system.

| Parameter	Value	Units
Number of pixels	256	
Spectral response range	340–780	nm
Spectral resolution	9	nm
Wavelength reproducibility	−0.5 to 0.5	nm
Wavelength temperature dependence	−0.05 to 0.05	nm °C^{-1}
Typical saturation voltage	3.2 (high gain), 2.5 (low gain)	V
Typical dark output voltage	2.0 (high gain), 0.4 (low gain)	mV
Fiber core diameter	600	μm
Operating temperature (no condensation)	5–40	°C

(a)

(b)
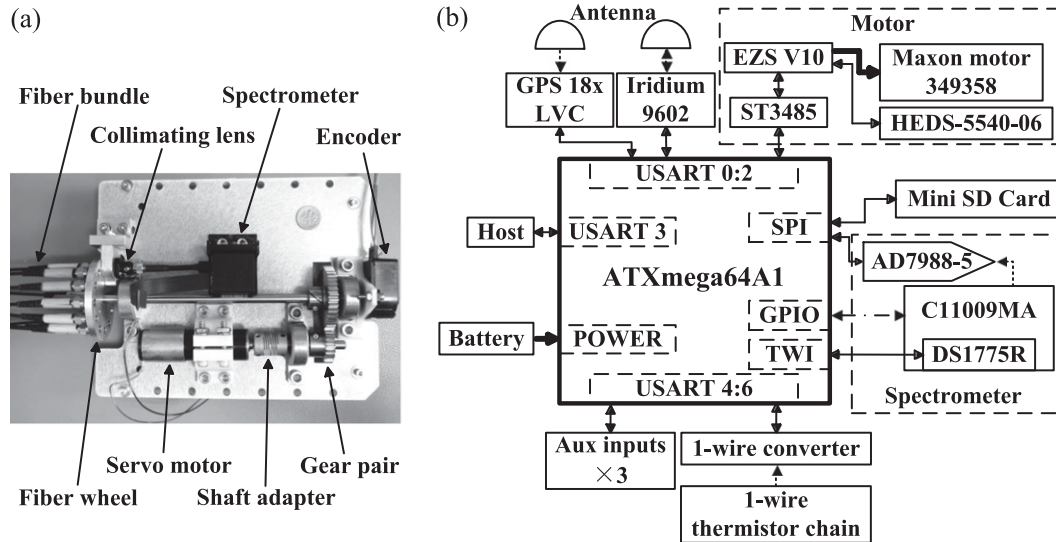
FIG. 2. (a) Physical arrangement of the spectrometer module and rotary fiber multiplexer. (b) Schematic of controller, sensors, and data flow for the in-ice spectrometry system. Solid arrows represent bidirectional digital communication, bold solid arrows represent power, dashed arrows represent data flow of the sensors and antennas, and dashed–dotted arrow represents logic-level connections.

directly to the shaft on which the fiber wheel is affixed and measures the angular position of the wheel. By attaching the encoder to the shaft with the fiber wheel, as opposed to the shaft with the motor, the fiber of interest can be more precisely aligned with input of the spectrometer module. This particular encoder generates 360 counts per revolution but through quadrature encoding, it can provide 4 times greater angular resolution of $\pm0.25°$. As the radius of the fiber wheel is 22 mm, the multiplexer has a maximum position precision of 0.1 mm, considerably smaller than the 5-mm diameter of the collimating lens used to couple the plastic fiber to the spectrometer input. This encoder additionally provides an index pulse that can be used to locate the absolute angular location of the fiber wheel.

A valuable advantage of employing a fiber-based spectrometer is the ability to use a wide range of optical fibers and/or probes at the end of each fiber. A very basic field application will involve measurement of both irradiance and radiance spectra, which can be accomplished by simply fitting different fibers with optical probes appropriate to these needs (e.g., a cosine or spherical diffusers for fibers measuring irradiance, and Gershun tubes for fibers measuring radiance). Fiber-end diffusers are available commercially [e.g., cosine corrector (CC)-3, Ocean Optics, Inc.], but we also explored the feasibility of designing small, custom diffuser geometries using 3D printing technology (Fig. 3). For our prototype system, we examined the use of plastic optical fiber, which has greater flexibility and a relatively smaller bend radius compared with a glass fiber of the same core diameter.

Bend radius is an important concern in our application, in order to meet our goal of deploying fiber probe bundles through a 5-cm auger hole. For our preliminary assessments, we used large-core (1000-μm diameter) polyethylene-jacketed acrylic optical fiber (02-536, Edmund Optics Inc.) that has good transmittance in the visible spectrum and can be conveniently cut and polished in the field.
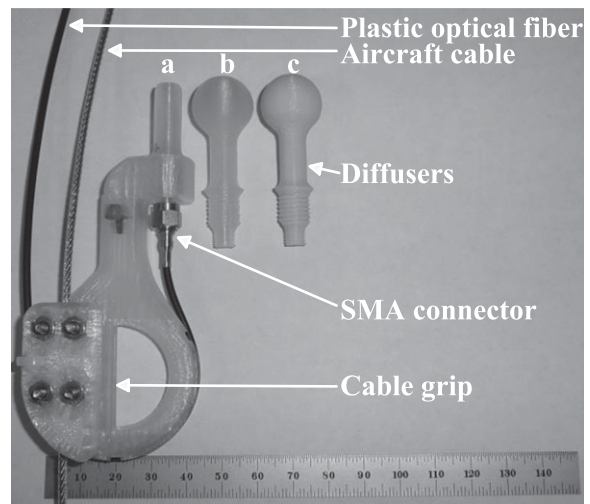

FIG. 3. Custom optical diffusers and fiber optic probe used in this study (material: polylactide). Different diffusers A–C can be fitted into the holder and attached to the fiber using standard screw mount assembly (SMA) connectors. Stainless steel aircraft cable is used as a strength member to locate multiple probes at precise depths within an auger hole or in the water column below.

c. System controller and electronic considerations

This spectrometer system is controlled by a low-power 8-bit microprocessor (ATXmega64A1, Atmel Corporation) that provides the timing and control signals needed to drive the spectrometer module (i.e., pixel clock pulse, integration time, and gain setting; Fig. 2b) and to control the 16-bit analog-to-digital converter (ADC) used to digitize the spectrometer module's output (AD7988–5, Analog Devices Inc.). No specific technical requirements were involved in the selection of this microprocessor beyond its range of usable clock speeds (see next section) and its complement of onboard peripherals, which simplified the integration of the various subsystems described below. To meet the timing requirements of this spectrometer module, this processor is clocked at 32 MHz, but the system clock is reduced between sampling intervals to decrease power consumption. We used the onboard 32-MHz resistor–capacitor (RC) oscillator as the clock source during prototyping for simplicity, but we recognize that other clock sources are available that have greater temperature stability, which could be incorporated into the design later if temperature-dependent biases due to clock stability are found to be an issue. The digitized voltages read from the spectrometer are transferred to the main processor over a serial peripheral interface (SPI) and are stored on a mini Secure Digital (SD) memory card. Necessary calibration information can be stored on the SD card or in the microprocessor's internal memory. The spectrometer module's temperature sensor is polled via a two-wire interface bus.

Control of the fiber wheel's drive motor and coordination with the rotary encoder is handled using a commercial servomotor controller (EZSV10, All Motion Inc.) through one of the microprocessor's serial ports. Another serial port is reserved for a short-burst data (SBD) Iridium satellite modem (9602, Iridium Communications Inc.) and another is provided for a GPS receiver (GPS-18x LVC, Garmin International, Inc.). Other serial ports are provided for ancillary sensors that would be valuable in envisioned field studies, such as a sonic ranging sensor (e.g., an SR50A, Campbell Scientific, Inc.), a sonar altimeter [e.g., a programmable sonar altimeter (PSA)-916, Teledyne Benthos, Inc.], or thermistor strings that operate on one-wire communication protocols (Maxim Integrated Products). A one-wire control module (LinkOEM, iButtonLink Technology) occupies one serial port in order to support one-wire peripherals, such as a high-resolution temperature chain.

The entire instrument runs off a battery pack whose voltage is monitored by an on-chip ADC within the microprocessor. Maximal power consumption (~3 W) occurs when the servomotor turns the fiber wheel, and minimal consumption in idle mode is ~0.3 W for the prototype in its current configuration.

3. Laboratory testing and evaluation

Because data regarding the temperature characteristics of this spectrometer module and the associated electronics are largely unavailable for the range of temperatures we specify for operation (down to −40°C), much of the following analysis focused on potential temperature dependence and biases of the spectrometer module and related circuitry. Temperature dependence in monolithic spectrometer modules can arise from mechanical distortion or stretching of the optical bench, or from characteristics of the module's internal electronics. Any such temperature dependence may in turn affect optical characteristics such as wavelength stability, CMOS sensor dark output, and linearity of the module. Careful evaluation of these potential sources of bias is essential in order to use any spectrometer module at the low environmental temperatures that can be expected to occur diurnally or seasonally in sea ice field studies. The Hamamatsu module we use here is specified for operation by the vendor down to only 5°C, whereas field deployments are expected to experience temperatures of at least −40°C. We examined the temperature dependence of the spectrometer module, the digitizing electronics, and the overall system behavior using an environmental test chamber (TestEquity 115A, TestEquity LLC) over a range of temperatures from −40° to 24°C. During these assessments we monitored the internal temperature sensor of the spectrometer module itself, and also that of the test chamber using a more accurate thermocouple (Fluke 80PK-1 and Fluke 87V, Fluke Inc.).

a. Temperature effect on spectrometer clock

The precision and stability of the spectrometer module's output signal depends ultimately on the precision and stability of the frequency of clock pulses (f_{CLK}) used to drive the spectrometer module. These pulses are generated by the microprocessor using its onboard 32-MHz RC oscillator, from which all internal timing signals are derived. We varied the temperature of the spectrometer system using the environmental chamber and measured the clock signal with an oscilloscope [mixed signal oscilloscope (MSO) 4034, Tektronix Inc.] over the 64°C range of temperatures between −40° to 24°C. We observed that f_{CLK}, which is nominally 196.4 kHz at 24°C, decreased linearly with increasing temperature from 201.9 kHz at −40°C to 196.4 kHz at 24°C ($f_{CLK} = a + bT$; $a = 198.5$ kHz, $b = -0.083\,84$ kHz °C^{-1}, $R^2 = 0.9981$, $n = 33$). This temperature effect is equivalent to a 0.042% decrease

in f_{CLK} per degree Celsius, which corresponds to at most a 2.8% maximum change over the full 64°C temperature span of operation. Although we only measured the clock signal used to drive the spectrometer, it is safe to assume that the same degree of temperature bias also propagates into other clock and timing signals produced by the microprocessor. In principle, it might be necessary to correct for this temperature bias in f_{CLK} depending on its magnitude compared to other sources of temperature-driven error. However, in this initial assessment we found that most other temperature-driven biases in the overall spectrometric measurements were much larger in comparison (detailed in the sections below). Therefore, for the following analyses, we ignore this relatively small temperature effect on f_{CLK} but recognize that it can be corrected for, if desired, or minimized further in future versions by using more stable clock sources.

b. Temperature effect on ADC system performance

When clocked by the microprocessor, the spectrometer module outputs a voltage level for each pixel of its internal CMOS linear sensor. These voltages are digitized by a 16-bit ADC and thus any potential temperature-dependent biases in this ADC may affect our measurements. We first examined the temperature dependence of the reference voltage (V_{ref}) provided to the ADC (5-V nominal; LM78M05C, Texas Instruments Inc.) using a 6.5-digit precision multimeter (Fluke 8845A, Fluke Inc.). Over the 64°C range of operating temperatures we examined, we observed a roughly parabolic temperature dependence in V_{ref} that could be well described by a second-order polynomial with a maximum at ~4°C (Fig. 4a). The maximum change in V_{ref} over this range of temperatures was not more than 7 mV, which corresponds to 92 counts as measured by the ADC.

We next examined temperature dependence in the overall ADC system—that is, the AD7955-5 in conjunction with its 5-V reference—using an ultralow-noise precision voltage reference chip (ADR431, Analog Devices, Inc.,) to generate an idealized voltage input. For this specific test, the spectrometer system control board was placed in the environmental test chamber and examined over the 64°C range of operating temperatures while holding the precision reference constant at room temperature (~24°C). To improve the precision of this assessment, ten repeated "scans" were performed at each temperature, where each scan involved 256 sequential conversions on this unchanging idealized input voltage, to mimic the clocking and noise that would occur when reading 256 pixels from the spectrometer module. To get the measured voltage V_{ADC} by the ADC system at each temperature, these 10 replicate scans were first averaged and divided by the ADC dynamic
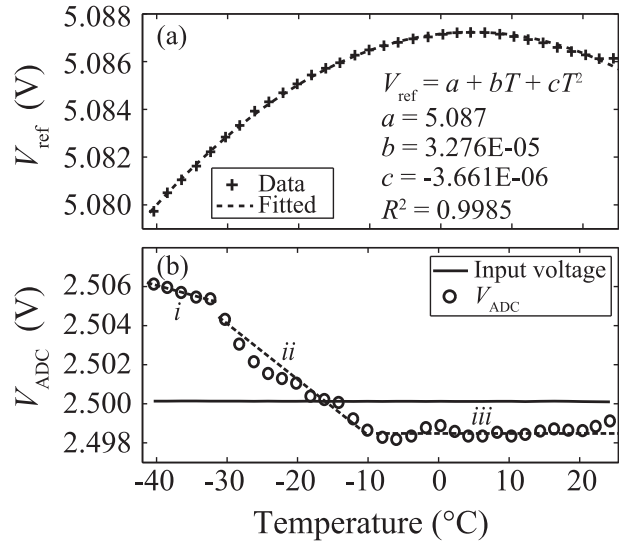

FIG. 4. Temperature dependence of (a) the ADC reference voltage and (b) the measured ADC output voltage. Three apparent phases are referenced in the text.

range of 2^{16} counts and then scaled by the reference voltage at the same temperature.

The temperature dependence in these ADC voltage measurements exhibited three apparent phases as a function of temperature, despite having a very stable input voltage (2.500 12 ± 0.000 02 V) provided as input to the ADC (Fig. 4b). At −40°C V_{ADC} was ~0.23% higher than expected, decreasing slightly as the temperature increased (phase 1). Above −32°C but below −10°C, the error in V_{ADC} became negative, at most 0.066% lower than expected at −10°C (phase 2). Above −10°C V_{ADC} was roughly stable at −0.066% of the expected value of 2.500 12 V (phase 3). These errors are all less than roughly ±0.25% over the entire range of expected operating temperatures and so are relatively negligible, but we note that they can be corrected for later, if desired.

c. Temperature effect on the pixel-to-wavelength relationship

The vendor-provided wavelength calibration for the C11009MA employs a fifth-order polynomial function to convert pixel number of the spectrometer module into wavelength (nm). This vendor calibration was performed at a single temperature (22.7°C), whereas our application will require operation over a wide range of temperatures, including well below freezing. We examined the temperature dependence of this module over our range of expected operational temperatures between −40° and 24°C using a standard mercury–argon calibration source (HG-1, Ocean Optics, Inc.) held at room temperature (~24°C). The mercury–argon source was coupled to the spectrometer system using a 2.5-m

TABLE 2. Correspondence of observed peaks (pixels) from known lines of a mercury–argon calibration source (nm). Parentheses indicate the two instances where the Hg–Ar lines at 546.074 and 750.387 nm registered—albeit infrequently—at one pixel above or below the typical reading.

Pixel position	Wavelength (nm)
22	365.015
43	404.656
59	435.833
119 (118)	546.074
136	579.066
201	696.543
232 (233)	750.387
245	772.376

length of the same 1000-μm plastic optical fiber described above, with no more than 5 cm of this fiber being placed in the temperature chamber during these tests, to minimize any artifact that might arise from temperature dependencies in the plastic fiber itself (which is examined separately below).

We collected 256-pixel scans of this calibration source, with the spectrometer module set at both high- and low-gain settings. Results from both gain settings were similar: across this entire range of temperatures, peaks in the mercury–argon emission were observed at the same pixels except for the peaks at 546.074 and 750.387 nm, which shifted by one pixel in only four instances for each of these peaks (Table 2). Using the vendor-provided calibration equation, this one-pixel shift predicts a shift in corresponding wavelength of at most 2 nm. Thus, over our range of expected operating temperatures, this spectrometer module maintains a reasonably consistent relationship between pixel and wavelength. In principle it is possible to develop a custom, temperature-resolved calibration function based on experimental data such as these observed mercury–argon pixel and wavelength pairs. Such a custom calibration might possibly improve upon the vendor-provided calibration but given our application, the vendor's calibration function is adequate.

d. Temperature effect on spectrometer dark output

The dark output of the spectrometer module (i.e., the voltage measured in the absence of light input) is a function of its dark voltage and offset voltage. Dark voltage arises from recombination current (dark current) within the photodiode depletion layer and the photodiode surface. Consequently, dark voltage is expected to be proportional to the integration time used in any given scan. Offset voltage is a function of the circuitry used within the spectrometer module to convert photodiode current to voltage, and because we have no access to this, we cannot separately examine the temperature effects on each of

these voltages. We therefore examined the temperature dependence of the module's dark output for both contributions to dark output together and used a statistical line-fitting approach to identify the individual contributions of each.

To do this we measured the module's dark output for 16 different integration times between 0.7 and 40 s, in both high- and low-gain modes, over our range of test temperatures between −40° to 24°C. In some measurements we noted anomalously high readings from pixels 1 and 256, so we considered only the 250 central pixels instead of the entire 256 in order to eliminate any artifact of this behavior in this particular analysis. The average dark output did not always increase as expected with longer integration times, and substantial variation was observed at different temperatures. At temperatures above −10°C, the slope of this relationship was higher and its intercept was lower, whereas for colder temperatures the slope was effectively zero but with higher intercepts (Fig. 5a). This suggests that dark output above −10°C is jointly affected by dark voltage and offset voltage, while at temperatures lower than −10°C dark output is dominated by offset voltage.

To quantify this behavior for use in future temperature correction schemes, we determined the slopes and intercepts of lines fitted to the integration time–dark output relationship for each of our 33 test temperatures, for both high- and low-gain settings (Figs. 5b,c). The intercepts of these relationships decreased linearly with temperature, which was expected given the offset voltage versus temperature relationships provided by the vendor (A. Yamauchi, Hamamatsu Photonics K.K., 2014, personal communication). In contrast, the slopes of these relationships exhibited a roughly exponential temperature dependence that is consistent with the expected exponential temperature dependence of photodiode dark current (Kuusk 2011). The temperature dependence of the intercept (i.e., influence of offset voltage) is very similar for both low- and high-gain measurements (Fig. 5b), whereas the temperature dependence of the slope (i.e., influence of dark current) differs strongly between low and high gain (Fig. 5c). The stronger temperature dependence seen with data collected in high-gain mode presumably results from the current-to-voltage amplifier within the spectrometer module, which amplifies the dark current more at high gain compared to low gain while not affecting offset voltage.

e. Temperature effects on spectrometer output beyond dark output

The output signal generated by the spectrometer module for each pixel is a function of a nonzero dark signal that occurs in the absence of light, and also of a light-dependent signal that in principle should be proportional
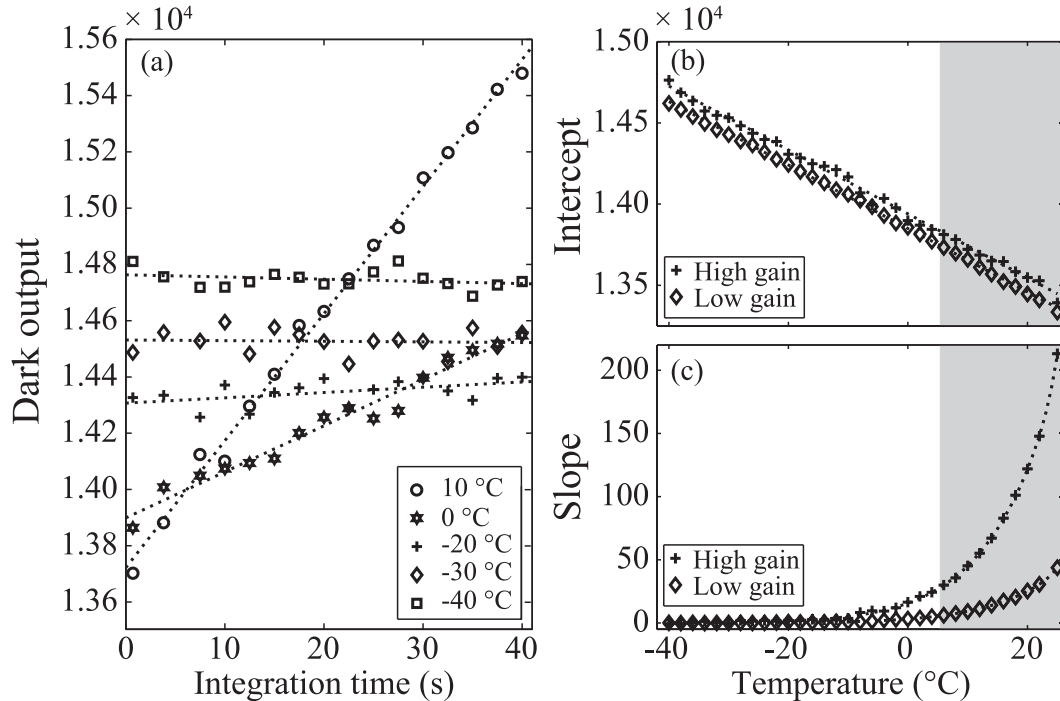
FIG. 5. Relationship between dark output and integration time at five temperatures in (a) high-gain mode, (b) the linear fitted intercepts, and (c) slopes of the relationship at all 33 test temperatures in both high- and low-gain modes. The shaded regions in (b) and (c) indicate temperatures within the vendor-specified range of operation. The dotted lines and curves indicate fits of the corresponding data.

to integration time for a constant illumination and ambient temperature. To identify any potential temperature-dependent biases that cannot be attributed to dark output, we examined the relationship between total output counts per pixel and integration time over our test temperature range (−40° to 24°C) while providing the spectrometer system with a constant light intensity. For this assessment we placed a standard PR4 miniature light-bulb as a light source outside the environmental test chamber at room temperature, and guided light from this source to the spectrometer inside the test chamber using the 1000-μm plastic fiber described above. A photodiode module (DET100, Thorlabs, Inc.) was used to monitor any changes in the output of this light source for subsequent correction in our analyses. We then measured the spectrometer's response to this light source, over a range of 20 integration times from 0.9 to 3.8 s in high-gain mode and from 4.4 to 21 s in low-gain mode, in order to keep the module's output signal below saturation. For completeness we also measured the corresponding dark outputs of this spectrometer for the same integration times, gain settings, and temperatures, in the absence of any external light source.

For purposes of analysis, it was necessary first to correct our light measurements for the dark output (by subtraction), and then normalize each measurement by

any variations in the intensity of the light source that may occur during data collection. For the purposes of this particular analysis, we also applied the vendor's pixel-to-wavelength calibration in order to examine our results in the context of the light source's spectral output. We also normalized all spectrometer data to the integration time used to collect these data, to be able to compare the results between scans made with different integration times. In these corrected measurements (counts per second), we observed that measured intensities differed very little for all the integration times at each test temperature and decreased with decreasing temperatures (Fig. 6a). Also, depending on the wavelength of interest, this relationship appeared weakly or moderately parabolic (Fig. 6b). This temperature dependence was well described by a second-order polynomial, and coefficients of these fits as a function of temperature provide a preliminary calibration framework that could in principle be later used to correct spectrometer measurements for temperature-dependent biases, beyond those already determined for dark output (Figs. 6c–e). Wavelengths where the correlation coefficients are poor for these fits (R^2 values $\ll 1$, that is, at λ shorter than 420 nm; Fig. 6f) presumably reflect poor fits due to weak signal intensities measured by the spectrometer in this range of wavelengths.
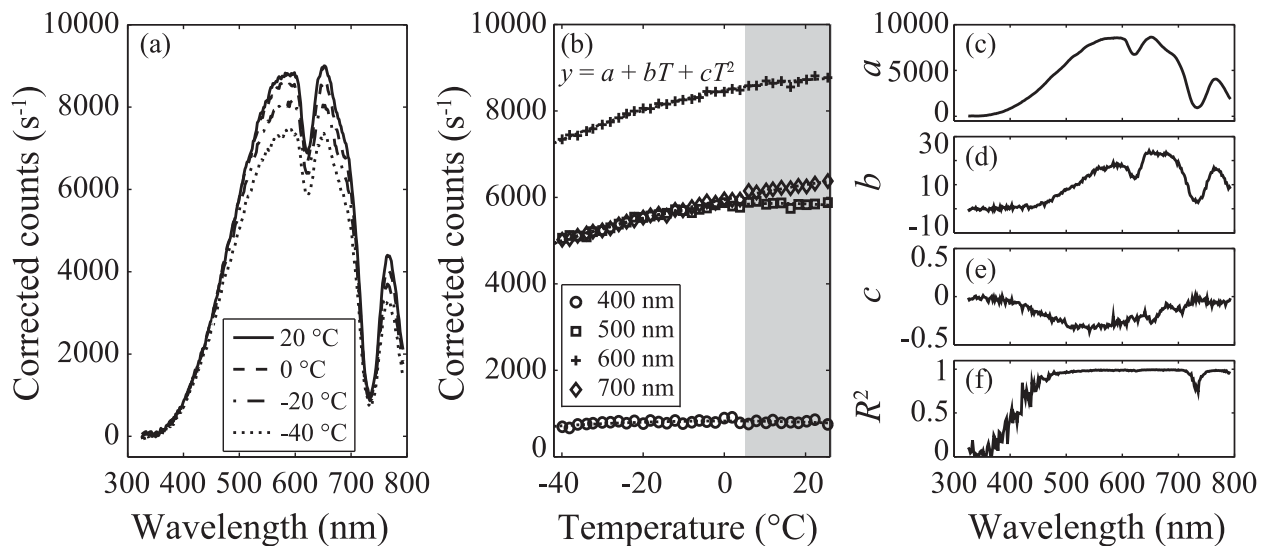
FIG. 6. Representative example of corrected measurements (per second) as a function of (a) wavelength at four demonstrative test temperatures and (b) temperature at four selected wavelengths. (c)–(e) The least squares fitted coefficients to a second-order polynomial and (f) the goodness of fit are shown for all wavelengths. All data used in this figure were measured in high-gain mode. Shaded regions in (b) are explained in Fig. 5.

f. Temperature effects on plastic optical fiber

Plastic optical fibers were preferred in our application because of their smaller bend radius and their relative ease of repair in field situations. However, temperature characteristics of such fibers are not well examined and plastic fibers introduce strong absorption at specific wavelengths that would not be seen in glass fibers. Both of these factors necessitated a better understanding of the spectral transmittance and temperature dependence of this plastic fiber. In our envisioned application (e.g., deployments similar to that in Fig. 1), the lengths of the various input fibers would vary considerably from 1 m to several meters. The vendor-supplied information regarding the typical attenuation of kilometer-length fibers is therefore not adequate for assessing the spectral attenuation on length scales of meters or any temperature dependences, necessitating a more detailed assessment.

We used the Hamamatsu spectrometer module to measure the spectral transmittance of this plastic optical fiber over our 64°C range of test temperatures, by providing the fiber with an input from a constant quartz tungsten halogen light source (6318, Newport Corporation) held at room temperature (~24°C). We examined two fibers: one of a length typical for our application (2.5 m) and one considerably longer (60 m). The purpose of examining this longer fiber is to identify any weak effects in temperature dependence that might not be evident with the shorter fiber but would compound and become more readily measured over longer fiber lengths. Any

fluctuations in the output of this tungsten halogen source during the course of these measurements were monitored by a reference photodiode (DET100, Thorlabs, Inc.). To improve statistical accuracy, we repeated our observations at each of these temperatures 35 times.

The spectral intensity measured with each fiber length (in ADC counts) was first corrected to remove the spectrometer's dark output and any observed fluctuations in the output of the tungsten halogen source as indicated by the reference photodiode. The corrected measurements were next divided by the integration time and averaged over the 35 replicate measurements. We then applied a spectral sensitivity correction that we determined for this particular spectrometer, generated from a side-by-side comparison study with a radiometrically calibrated hyperspectral sensor [hyperspectral ocean color radiometer (HyperOCR), Satlantic LP] used as a standard. Then we normalized each of the measurement to be able to compare the spectral absorption characteristic of the two fibers directly. With this approach it was possible to see that the tungsten halogen light source emitted a broad smooth spectrum that continues to rise into the infrared wavelengths, but the 2.5-m fiber introduces significant absorption around 621, 732, and broadly longer than 650 nm (Fig. 7a). When examining the much longer 60-m fiber, weaker absorption bands around 545 and below 500 nm became more apparent. These spectral transmittance characteristics are broadly consistent with the vendor-provided attenuation spectra for this plastic fiber, but our observations provide a more accurate assessment of spectral attenuance at fiber lengths appropriate for our field application.
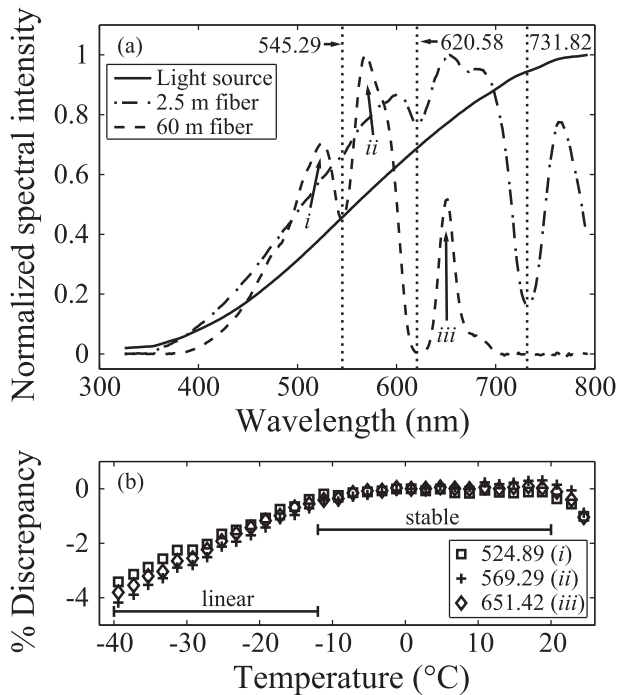
FIG. 7. (a) Normalized spectral intensity of the light source and the light as transmitted by two lengths of fiber (2.5 and 60 m) held at 0°C. (b) Examples of three selected wavelengths of temperature dependence in the intensity transmitted by the 60-m fiber, corresponding to the three peaks indicated in the spectrum in (a), taking 0°C as a reference.

These plastic fibers exhibited two main temperature dependences within the range of test temperatures we examined. These dependences are most clearly quantified using the 60-m fiber and at wavelengths where the transmitted intensity is strongest (e.g., ~525, 569, and 651 nm; phases 1–3 in Fig. 7a). Below approximately −12°C, the transmittance of this fiber decreased roughly linearly with decreasing temperature (Fig. 7b), with the biggest decrease from 0% to −6% (referenced to 0°C) observed between −12° and −40°C. In contrast, above −10°C the response was generally stable with temperature at ±1% (referenced to 0°C) until around 20°C. Although we here describe this temperature dependence at only three wavelengths, we note that this general pattern holds over the entire range of wavelengths we examined where intensity was meaningfully above zero.

Given a simple Beer–Lambert model for attenuation as a function of fiber length, we can use these results from the 60-m fiber to estimate the temperature effects on shorter fibers that would be more typical in a field deployment scenario. We estimate that transmittance in a 2.5-m fiber will decrease approximately 0.3% as ambient temperature decreases from −12° to −40°C. This is slightly less than the actual decrease in transmittance we observed in the actual 2.5-m fiber (0.5%). For the longest fiber we might expect to use in the field (~10 m), the temperature effect on attenuation would be around 1% at most. In practice it will be difficult to determine exactly the temperature effects of fibers used in any field application, given that each fiber will have some length in air, some in the snow, and some embedded in sea ice.

There are additional aspects of plastic optical fiber that would be important in our field application beyond just temperature dependence, most notably the bend radius. The smallest recommended bend diameter of the specific fiber we used (110 mm) is bigger than our idealized 2-in.-diameter auger hole. Thus, any effect of macrobending on fiber attenuation might be significant, but a preliminary laboratory examination indicated that the light signal lost only ~7% due to this particular bend. However, this value might differ somewhat between fiber-and-diffuser probe combinations and so probes may need to be tested and calibrated individually to quantify any probe-to-probe differences. It is also possible that other custom-printed diffuser designs could be developed to further minimize or eliminate losses due to bending.

g. Mechanical repeatability at subzero temperatures

Good repeatability in aligning the various input fibers to the spectrometer module is important for a multifiber sampling system. The efficiency of this coupling is determined by the numerical apertures of the fibers, the collimation lens used to couple the fibers, and the accuracy of the motor subsystem that rotates the fiber wheel. This entire system may be affected by temperature, if changes in temperature materially alter the mechanical alignment of the fiber or the fiber coupling, or if they introduce variations in friction in the mechanical components. We examined the repeatability of the fiber multiplexer at four temperatures (20°, 0°, −20°, and −40°C) by measuring the intensity of light guided by one fiber in the wheel as it was repeatedly rotated in and out of alignment with the aperture for the spectrometer module's fiber input. Substituting for the module, a second fiber with the same core diameter as the spectrometer was connected to the collimating lens, with another end connected to a photodiode (DET100, Thorlabs, Inc.) to measure changes in coupled light intensity during these repeated rotations. Potential fluctuations in the light source used in this assessment were monitored by a reference photodiode [amplified photodetector (PDA) 150, Thorlabs, Inc.] for completeness. For each of the four test temperatures, we observed little variability in measured light intensity (Table 3), indicating that the fiber multiplexer had adequate position repeatability and displayed

TABLE 3. Measures of mechanical repeatability at four test temperatures, including the coefficient of variation (CV), mean, and standard deviation.

Temp (°C)	CV (%)	Mean (V)	Std dev (V)
20	0.1264	0.1229	1.553×10^{-4}
0	0.065 33	0.1223	7.990×10^{-5}
−20	0.073 28	0.1205	8.830×10^{-5}
−40	0.1288	0.1190	1.533×10^{-4}

little influence of temperature over our range of expected working temperatures.

4. Assessment in simulated ice columns

To assess the performance of this spectrometer system in laboratory conditions, we froze four optical probes (Fig. 3, diffuser type A) and corresponding fibers within a vertical 1.2-m-tall column of ice with a 12-in. diameter. The topmost of these probes was located 0.01 m below the ice surface and the remaining three were distributed deeper in the central axis of the column on 0.25-m intervals (Fig. 8a). We illuminated the ice column from above with a 75-W incandescent lightbulb (Sylvania 211, Osram Sylvania) and measured the spectral intensity of each probe as a function of depth within the ice while holding the spectrometer system at room temperature. This bulb illuminated the top of the ice column with $\sim$20 W m^{-2} of light energy ($\sim$100 μmol photons m^{-2} s^{-1}), which is comparable to the incident PAR irradiance measured in a field study in July–August in the Arctic above 80°N (Gosselin et al. 1997). Any fluctuations in the light source output were monitored by a reference photodiode (DET100, Thorlabs, Inc.). The spectral intensity of this light source was measured concurrently using a radiometrically calibrated hyperspectral sensor (HyperOCR, Satlantic LP) to determine the absolute incident irradiance entering the top surface of the ice column.

Given the strong attenuation with depth of the illuminating light in this ice column, increasingly longer integration times were needed to measure the light sampled by probes located deeper in the ice. Integration time ranged from 3.9 s for the top fiber to 72.2 s for the bottom fiber (Figs. 8b–e). To reduce the noise in these measurements, repeated scans were performed at each depth: 10 each for the top two probes and 90 each for the bottom two probes. The signal-to-noise ratio (SNR) of these measurements was computed by separating the pixel-to-pixel noise from the general spectral trend (using a five-element running average filter over these 256 pixels), and then dividing the signal intensity at a wavelength near the spectral maximum (we chose 600 nm) by the root-mean-square of

the measured noise. The SNR decreased notably for probes deeper in the ice, where less signal was present (SNR: $\sim$460 for probe 1 at the top of the ice column; $\sim$3 for probe 4 at 0.76-m depth in the ice).

We next corrected the spectral measurements of each fiber probe to remove dark output and fluctuations in the light source, and then averaged over the number of scans collected. Then we scaled these data with respect to integration time and corrected for differences in spectral sensitivity among each of the four fiber probes, using the same radiometrically calibrated hyperspectral sensor as a standard. This provides us with radiometric spectra in the ice (μW cm^{-2} nm^{-1}). From these spectra we observed that irradiance intensity dropped dramatically with increasing depth in the ice (Figs. 8b–e, solid lines) and that the spectral irradiance measurements from the deepest probe (probe 4) were very noisy. Yet the general shape of the spectrum seen by this deepest probe was still discernable and similar to that measured higher in the ice column (i.e., probes 2 and 3). The seemingly noisier measurements seen at wavelengths outside of 400–700 nm (e.g., Figs. 8c–e) can be explained by the lower spectral sensitivity of this system (spectrometer module plus fiber) in the ultraviolet or infrared wavelengths.

In our simulated sea ice column, the incident light displayed a broad smooth spectrum (as measured with the hyperspectral reference radiometer; Fig. 8b, dashed line), but as this light propagated through the column, significant absorption was observed at wavelengths above 700 nm. This phenomenon became more apparent with the deeper probes and agreed well with the spectral absorption property of pure ice, which absorbs much more infrared than the visible light (Warren et al. 2006). To obtain a preliminary estimate of the system's overall sensitivity in simulated sea ice, we calculated the integrated irradiance intensity I_z at each depth using the corrected irradiance measurement in the visible wavelengths only (400–700 nm; shaded regions in Figs. 8b–e). We observed that these integrated I_z decreased deeper into the ice column, roughly exponentially with depth (I_z: $\sim$1050 μW cm^{-2} for probe 1; $\sim$0.25 μW cm^{-2} for probe 4 in the ice; Fig. 8f) as would be expected for a homogeneous ice column that approximates attenuation following the Beer–Lambert law. None of our four fibers gave measurements that significantly deviated from exponential attenuation, indicating good relative accuracy between each of the four probes. The integrated intensity measured at probe 1 in the ice column was roughly half of that of the incident light ($\sim$2070 μW cm^{-2}, between 400 and 700 nm), presumably because of reflection at the ice surface, and absorption and scattering within the ice. The absolute intensity measured by the deepest probe was
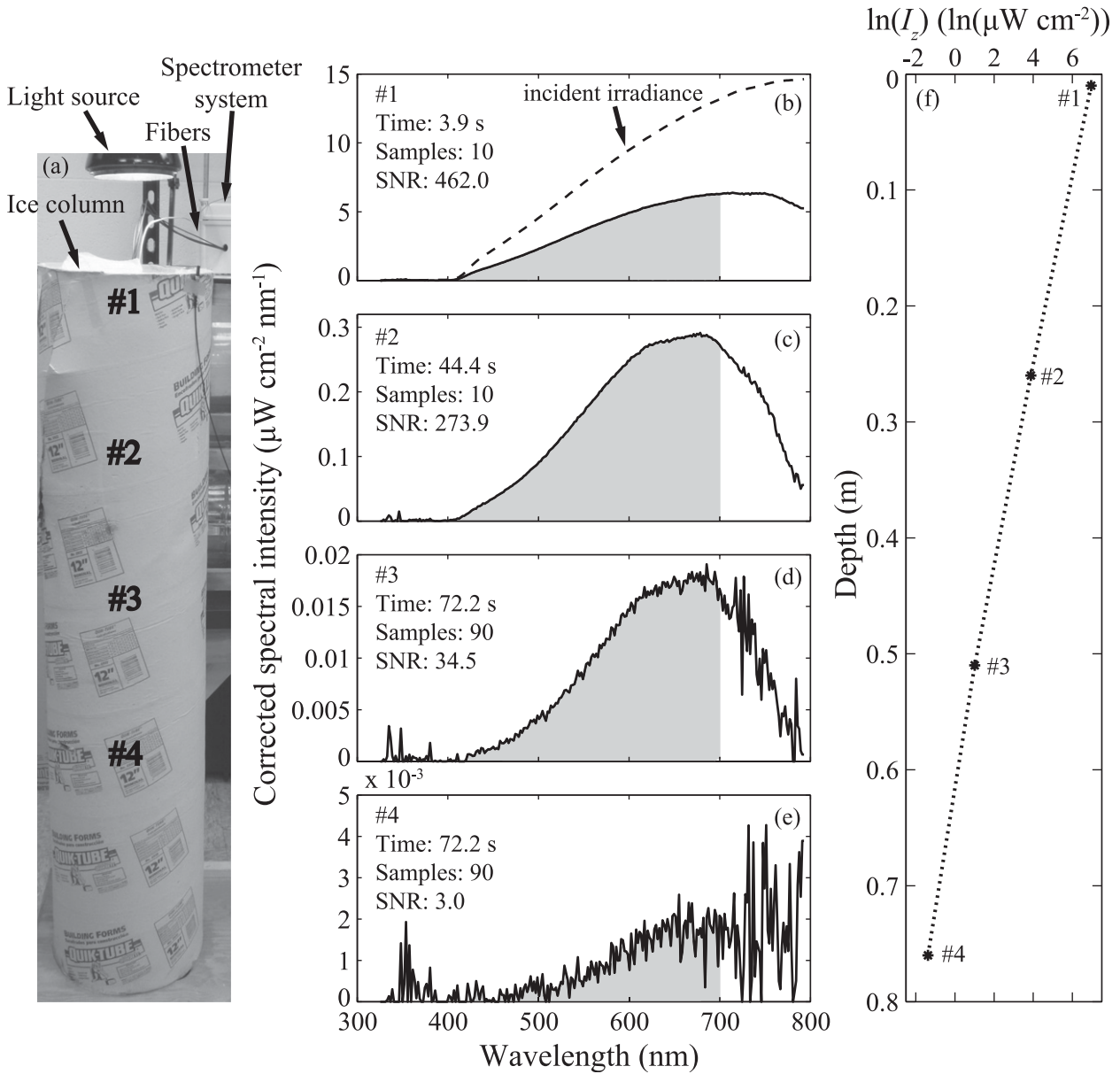
FIG. 8. (a) Photograph of a simulated ice core, illuminated by a light source, indicating the location of four probes (1–4) frozen into the core. (b)–(e) Corrected spectral intensity as a function of wavelength for probes 1–4, with shaded regions indicating the wavelengths over which I_z was calculated for panel (f). (f) Integrated intensity as a function of depth within the ice column.

$\sim 0.25\,\mu\mathrm{W\,cm}^{-2}$ over the range of 400–700 nm, which corresponded to an average noise-equivalent irradiance (NEI) of at most $\sim 0.85 \times 10^{-3}\,\mu\mathrm{W\,cm}^{-2}\,\mathrm{nm}^{-1}$. This might be an underestimation because we have not corrected for the immersion factor of the probe ends (which will be assessed in later studies), yet this sensitivity is likely close to that of the commercial calibrated hyperspectral radiometer we used as a standard in this assessment (NEI: $1.5 \times 10^{-3}\,\mu\mathrm{W\,cm}^{-2}\,\mathrm{nm}^{-1}$). Furthermore, because we are able to obtain a measurable signal at the deepest probe used in this study, we believe the actual NEI of this

spectrometer system should be even lower. Naturally, ice thickness and daily and seasonal fluctuations in incident solar irradiance will introduce situations when light levels are too low to be measured by this or any instrument, but for use in the Arctic this system appears to be sensitive enough. Irradiance intensities measured in the ocean below snow-covered, meter-thick ice (e.g., Maykut and Grenfell 1975; Nicolaus et al. 2010a) are well above the signal floor of this prototype, suggesting it will perform comparably to, if not better than, current approaches for assessing expected in-ice irradiance

intensities. The performance of this fiber-based spectrometer system could potentially be improved further by developing better optical probes, choosing more appropriate fibers with less attenuation in specific wavelengths (e.g., as seen in Fig. 7a), or by performing daily sampling around solar noon maxima.

5. Conclusions

The fiber-based spectrometry system that we describe here represents one approach for measuring spectral irradiance from multiple depths within a layer of sea ice, potentially over seasonal or annual time scales if applied in an autonomous scenario. The prototype system is low cost (~$5000 per unit in components) and relatively easy to manufacture and deploy in the field. It uses a single spectrometer module multiplexed to up to 12 optical fibers, but in principle the number of fibers sampled is limited only by the physical design of the multiplexer wheel used to couple these fibers to the spectrometer module. This system has been tested at temperatures well below the vendor-specified minimum operating temperatures, and test results indicate that temperature-induced variances in both dark output and spectral output can be adequately compensated. Such detail in characterizing the temperature biases is necessary for robust use of this system in the field, where ambient temperatures are expected to vary considerably over seasonal or annual scales.

Our assessment in a simulated ice column indicated that this prototype system has adequate performance to warrant further refinement for application in actual field experiments. Our results suggest that the spectrometer system can measure spectral irradiance at integrated intensities as low as $\sim 0.25 \,\mu\mathrm{W\,cm}^{-2}$ (400–700 nm), although measuring wavelengths between 400 and 450 nm becomes increasingly difficult with decreasing intensities in those wavelengths. Although these results are promising, several aspects of this system might benefit from improvement. First, better optical probes could provide us a much stronger light signal at the same illumination environment, which is necessary for our application because of the generally low irradiance intensities found within sea ice. This may involve better fibers, better probe diffusers, or combinations of the two. Second, a more sophisticated understanding of the temperature behavior of the various electrical and optical components might help to improve the accuracy of irradiance measurements. We have examined the first-order biases that arise from changes in temperature, but longer-term changes in stability or sensitivity have not yet been examined and could potentially be a problem. Most importantly, long-term drift is not addressed in the manufacturer's specifications for the

monolithic spectrometer used in this study and should be examined in more detail in future studies. Third, for any widespread use in polar regions, it will be necessary to standardize our approach for characterizing the behavior of these instruments, perhaps to distinguish general biases from those that require instrument-specific characterization and compensation. These possible avenues for improvement notwithstanding, this fiber optic–based spectrometry system shows considerable promise for expanding our ability to examine spectral irradiance and associated properties in sea ice, over the seasonal time scales that are highly relevant to sea ice algal communities.

REFERENCES

Arrigo, K. R., and D. Thomas, 2004: Large scale importance of sea ice biology in the Southern Ocean. *Antarct. Sci.,* **16,** 471–476, doi:10.1017/S0954102004002263.

Ehn, J. K., C. J. Mundy, and D. G. Barber, 2008: Bio-optical and structural properties inferred from irradiance measurements within the bottommost layers in an Arctic landfast sea ice cover. *J. Geophys. Res.,* **113,** C03S03, doi:10.1029/2007JC004194.

Frey, K. E., D. K. Perovich, and B. Light, 2011: The spatial distribution of solar radiation under a melting Arctic sea ice cover. *Geophys. Res. Lett.,* **38,** L22501, doi:10.1029/2011GL049421.

Fritsen, C. H., V. I. Lytle, S. F. Ackley, and C. W. Sullivan, 1994: Autumn bloom of Antarctic pack-ice algae. *Science,* **266,** 782–784, doi:10.1126/science.266.5186.782.

——, E. D. Wirthlin, D. K. Momberg, M. J. Lewis, and S. F. Ackley, 2011: Bio-optical properties of Antarctic pack ice in the early austral spring. *Deep-Sea Res. II,* **58,** 1052–1061, doi:10.1016/j.dsr2.2010.10.028.

Gosselin, M., M. Lavasseur, P. A. Wheeler, R. A. Horner, and B. C. Booth, 1997: New measurements of phytoplankton and ice algal production in the Arctic Ocean. *Deep-Sea Res. II,* **44,** 1623–1644, doi:10.1016/S0967-0645(97)00054-4.

Grenfell, T. C., and D. K. Perovich, 1984: Spectral albedos of sea ice and incident solar irradiance in the southern Beaufort Sea. *J. Geophys. Res.,* **89,** 3573–3580, doi:10.1029/JC089iC03p03573.

Haas, C., D. N. Thomas, and J. Bareiss, 2001: Surface properties and processes of perennial Antarctic sea ice in summer. *J. Glaciol.,* **47,** 613–625, doi:10.3189/172756501781831864.

Jackson, K., J. Wilkinson, T. Maksym, D. Meldrum, J. Beckers, C. Haas, and D. Mackenzie, 2013: A novel and low-cost sea ice mass balance buoy. *J. Atmos. Oceanic Technol.,* **30,** 2676–2688, doi:10.1175/JTECH-D-13-00058.1.

Karentz, D., J. E. Cleaver, and D. L. Mitchell, 1991: Cell survival characteristics and molecular responses of Antarctic phytoplankton to ultraviolet-B radiation. *J. Phycol.,* **27,** 326–341, doi:10.1111/j.0022-3646.1991.00326.x.

Kuusk, J., 2011: Dark signal temperature dependence correction method for miniature spectrometer modules. *J. Sens.,* **2011,** 608157, doi:10.1155/2011/608157.

Legendre, L., M.-J. Martineau, J.-C. Therriault, and S. Demers, 1992: Chlorophyll a biomass and growth of sea-ice microalgae along a salinity gradient (southeastern Hudson Bay, Canadian Arctic). *Polar Biol.,* **12,** 445–453.

Light, B., T. C. Grenfell, and D. K. Perovich, 2008: Transmission and absorption of solar radiation by Arctic sea ice during the melt season. *J. Geophys. Res.,* **113,** C03023, doi:10.1029/2006JC003977.

Maksym, T., and M. O. Jeffries, 2001: Phase and compositional evolution of the flooded layer during snow-ice formation on Antarctic sea ice. *Ann. Glaciol.,* **33,** 37–44, doi:10.3189/172756401781818860.

Maykut, G. A., and T. C. Grenfell, 1975: The spectral distribution of light beneath first-year sea ice in the Arctic Ocean. *Limnol. Oceanogr.,* **20,** 554–563, doi:10.4319/lo.1975.20.4.0554.

Mundy, C. J., J. K. Ehn, D. G. Barber, and C. Michel, 2007: Influence of snow cover and algae on the spectral dependence of transmitted irradiance through Arctic landfast first-year sea ice. *J. Geophys. Res,* **112,** C03007, doi:10.1029/2006JC003683.

Nicolaus, M., and C. Katlein, 2013: Mapping radiation transfer through sea ice using a remotely operated vehicle (ROV). *Cryosphere,* **7,** 763–777, doi:10.5194/tc-7-763-2013.

——, S. Gerland, S. R. Hudson, S. Hanson, J. Haapala, and D. K. Perovich, 2010a: Seasonality of spectral albedo and transmittance as observed in the Arctic Transpolar Drift in 2007. *J. Geophys. Res.,* **115,** C11011, doi:10.1029/2009JC006074.

——, S. R. Hudson, S. Gerland, and K. Munderloh, 2010b: A modern concept for autonomous and continuous measurements of spectral albedo and transmittance of sea ice. *Cold Reg. Sci. Technol.,* **62,** 14–28, doi:10.1016/j.coldregions.2010.03.001.

——, C. Katlein, J. Maslanik, and S. Hendricks, 2012: Changes in Arctic sea ice result in increasing light transmittance and absorption. *Geophys. Res. Lett.,* **39,** L24501, doi:10.1029/2012GL053738.

Palmisano, A. C., J. Beeler SooHoo, R. L. Moe, and C. W. Sullivan, 1987: Sea ice microbial communities. VII. Changes in under-ice spectral irradiance during the development of Antarctic sea ice microalgal communities. *Mar. Ecol.: Prog. Ser.,* **35,** 165–173, doi:10.3354/meps035165.

Perovich, D. K., G. F. Cota, G. A. Maykut, and T. C. Grenfell, 1993: Bio-optical observations of first-year Arctic sea ice. *Geophys. Res. Lett.,* **20,** 1059–1062, doi:10.1029/93GL01316.

——, C. S. Roesler, and W. S. Pegau, 1998: Variability in Arctic sea ice optical properties. *J. Geophys. Res.,* **103,** 1193–1208, doi:10.1029/97JC01614.

——, T. C. Grenfell, B. Light, and P. V. Hobbs, 2002: Seasonal evolution of the albedo of multiyear Arctic sea ice. *J. Geophys. Res.,* **107,** 8044, doi:10.1029/2000JC000438.

Richter-Menge, J. A., D. K. Perovich, B. C. Elder, K. Claffey, I. Rigor, and M. Ortmeyer, 2006: Ice mass-balance buoys: A tool for measuring and attributing changes in the thickness of the Arctic sea-ice cover. *Ann. Glaciol.,* **44,** 205–210, doi:10.3189/172756406781811727.

Saenz, B. T., and K. R. Arrigo, 2012: Simulation of a sea ice eco-system using a hybrid model for slush layer desalination. *J. Geophys. Res.,* **117,** C05007, doi:10.1029/2011JC007544.

Warren, S. G., R. E. Brandt, and T. C. Grenfell, 2006: Visible and near-ultraviolet absorption spectrum of ice from transmission of solar radiation into snow. *Appl. Opt.,* **45,** 5320–5334, doi:10.1364/AO.45.005320.